Deep Learning to Segment Pelvic Bones: Large-scale CT Datasets and Baseline Models

Pengbo Liu · Hu Han · Yuanqi Du · Heqin Zhu · Yinhao Li · Feng Gu · Honghu Xiao · Jun Li · Chunpeng Zhao · Li Xiao · Xinbao Wu · S.Kevin Zhou

Received: date / Accepted: date

Abstract Purpose: Pelvic bone segmentation in CT has always been an essential step in clinical diagnosis and surgery planning of pelvic bone diseases. Existing methods for pelvic bone segmentation are either hand-crafted or semi-automatic and achieve limited accuracy when dealing with image appearance variations due to the multi-site domain shift, the presence of contrasted vessels, coprolith and chyme, bone fractures, low dose, metal artifacts, etc. Due to the lack of a large-scale pelvic CT dataset with annotations, deep learning methods are not fully explored. Methods: In this paper, we aim to bridge the data gap by curating a large pelvic CT dataset pooled from multiple sources and different manufacturers, including 1, 184 CT volumes and over 320,000 slices with different resolutions and a variety of the above-mentioned appearance variations. Then we propose for the first time, to the best of our knowledge, to learn a deep multi-class network for segmenting lumbar spine, sacrum, left hip, and right hip, from multiple-domain images simultaneously to obtain more effective and robust feature representations. Finally, we introduce a post-processing tool based on the signed distance function (SDF) to eliminate false predictions while retaining correctly predicted bone fragments. Results: Extensive experiments on our dataset demonstrate the effectiveness of our automatic method, achieving an average Dice of 0.987 for a metal-free volume. SDF post-processor yields a decrease of 10.5% in hausdorff distance by maintaining important bone fragments in post-processing phase. Conclusion: We believe this large-scale dataset will promote the development of the whole community and plan to open source the images, annotations, codes, and trained baseline models at this URL¹.

Pengbo Liu, Hu Han, Heqin Zhu, Yinhao Li, Feng Gu, Jun Li, Li Xiao, S.Kevin Zhou Institute of Computing Technology, Chinese Academy of Sciences

Honghu Xiao, Chunpeng Zhao, Xinbao Wu Beijing Jishuitan Hospital

Yuanqi Du George Mason University

Feng Gu

Beijing Electronic Science and Technology Institute

https://github.com/ICT-MIRACLE-lab/CTPelvic1K

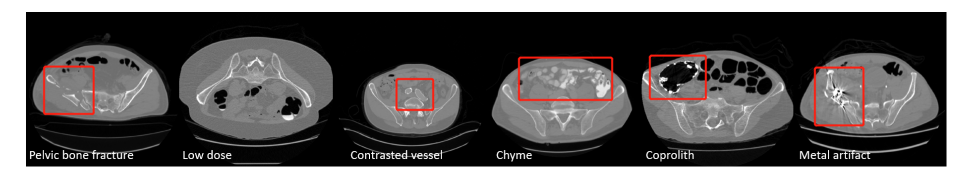


Fig. 1 Pelvic CT image examples with various conditions.

Keywords CT dataset · pelvic segmentation · SDF post-processing

1 Introduction

The pelvis is an important structure connecting the spine and lower limbs and plays a vital role in maintaining the stability of the body and protecting the internal organs of the abdomen. The abnormality of the pelvis, like hip dysplasia [18] and pelvic fractures [2], can have a serious impact on our physical health. For example, pelvic fractures that account for about 3% of all orthopedic injuries [10] are the most severe and life-threatening bone injuries with high mortality and morbidity [25]. Pelvic fractures are mainly caused by high energy blunt trauma, like road traffic accidents (RTAs) and fall from height, even though sometimes injuries come from low energy mechanism (i.e., frail and elderly patients fall). Moreover, patients with pelvic fractures are often accompanied by concomitant injuries, such as internal abdominal and pelvic viscera damages, which increase the overall morbidity and mortality. Compared with the overall pelvic fractures mortality rate of 3%-16%, the mortality rate of the elderly reaches 20% and the mortality rate of the open pelvic fractures is as high as 45% [7,11].

Medical imaging plays an important role in the whole process of diagnosis and treatment of patients with pelvic injuries. Compared with X-Ray images, CT images can provide more details about the damaged site to surgeons, such as cracks of the sacrum, acetabular fractures, and internal bleeding during the diagnosis stage. CT preserves the actual anatomic structure including depth information, so it is often used for 3D reconstruction to make follow-up **surgery planning** and evaluation of postoperative effects. In these applications, **accurate pelvic bone segmentation** is crucial for assessing the severity of pelvic injuries and helping surgeons to make correct judgments and choose the appropriate surgical approaches. In the past, surgeons segmented pelvis manually from CT using software like Mimics², which is time-consuming and non-reproducible. To address these clinical needs, we here present an automatic algorithm that can accurately and quickly segments pelvic bones from CT.

Existing methods for pelvic bone segmentation from CT mostly use simple thresholding [1], region growing [33], and handcrafted models, which include deformable models [17,32], statistical shape models [30,19], watershed [35] and others [26,12,22,8,23,4]. These methods focus on local gray information and have limited accuracy due to the weak density differences between cortical and trabecular bones. While cortical bone is smooth with high intensity in CT image,

https://en.wikipedia.org/wiki/Mimics

trabecular bone has a spongy texture and an intensity similar to that of the surrounding tissues. Bone fractures, if present, further lead to weak edges. Recently, deep learning-based methods [24,29,15,36,5,6,37,9] have achieved great success in image segmentation; however, their effectiveness for CT pelvic bone segmentation is not fully known. Although there are some datasets related to pelvic bone [20,34,14,3], only a few of them are open-sourced and with small size (less than 5 images or 200 slices), far less than other organs [13,31]. Although [14] conducted experiments based on deep learning, the result was not very good (Dice=0.92) with the dataset only having 200 CT slices. For the robustness of the deep learning method, it is essential to have a comprehensive dataset that includes as many real scenes as possible. In this paper, we bridge this gap by curating a large-scale CT dataset and explore the use of deep learning in this task, which marks, to the best of our knowledge, the first real attempt in the literature.

To build a comprehensive dataset, we have to deal with diverse image appearance variations due to differences in imaging resolution and field-of-view (FOV), domain shift arising from different sites, the presence of contrasted vessels, coprolith and chyme, bone fractures, low dose, metal artifacts, etc. Fig. 1 gives some examples about these various conditions. Among the above-mentioned appearance variations, the challenge of the metal artifacts is the most difficult to handle. Further, we aim at a multi-class segmentation problem that separates the pelvis into multiple bones, including lumbar spine, sacrum, left hip, and right hip, instead of simply segmenting out the whole pelvis from CT.

The contributions of this paper are summarized as follows:

- A pelvic CT dataset pooled from multiple domains and different manufacturers, including 1,184 CT volumes (over 320K CT slices) of diverse appearance variations (including 75 CTs with metal artifacts). Their multi-bone labels are carefully annotated by experts. We plan to make it open source to benefit the whole community;
- Learning a deep multi-class segmentation network [15] to obtain more effective representations for joint lumbar spine, sacrum, left hip, and right hip segmentation from multi-domain labeled images, thereby yielding desired accuracy and robustness:
- A fully automatic analysis pipeline that achieves high accuracy, efficiency, and robustness, thereby enabling its potential use in clinical practices.

2 Our Dataset

2.1 Data Collection

To build a comprehensive pelvic CT dataset that can replicate practical appearance variations, we curate a large dataset of pelvic CT images using the following seven sources.

<u>CLINIC</u> and <u>CLINIC-metal</u>. These two sub-datasets are related to pelvic fractures collected from an orthopedic hospital we collaborate with. CLINIC is collected from preoperative images without metal artifact, and CLINIC-metal is mainly collected from postoperative images with metal artifacts.

<u>KITS19.</u> This sub-dataset is from the Kits19 challenge [13] which is related to kidney and kidney tumor segmentation.

Table 1 Overview of our large-scale Pelvic CT dataset. 'Tr/Val/Ts' denotes training/validation/testing set. Ticks $[\checkmark]$ in table refer to we can access the CT images' acquisition equipment manufacturer [M] information of that sub-dataset. Due to the difficulty of labeling the CLINIC-metal, CLINIC-metal is taken off in our supervised training phase.

Dataset name[M]	#	Mean spacing(mm)	Mean size	# of Tr/Val/Ts	Source and Year
ABDOMEN	35	(0.76, 0.76, 3.80)	(512, 512, 73)	21/7/7	website ³ 2015
COLONOG[√]	731	(0.75, 0.75, 0.81)	(512, 512, 323)	440/146/145	[16] 2008
MSD_T10	155	(0.77, 0.77, 4.55)	(512, 512, 63)	93/31/31	[31] 2019
KITS19	44	(0.82, 0.82, 1.25)	(512, 512, 240)	26/9/9	[13] 2019
CERVIX	41	(1.02, 1.02, 2.50)	(512, 512, 102)	24/8/9	website ³ 2015
CLINIC[✓]	103	(0.85, 0.85, 0.80)	(512, 512, 345)	61/21/21	Clinical data
CLINIC-metal[✓]	75	(0.83, 0.83, 0.80)	(512, 512, 334)	0(61)/0/14	Clinical data
Our Datasets	1 184	(0.78 0.78 1.46)	(512, 512, 273)	665(61)/222/236	_

<u>CERVIX and ABDOMEN.</u> These two sub-datasets are from the Multi-Atlas Labeling Beyond the Cranial Vault – Workshop and Challenge³. They are all multi-organ segmentation datasets for different body regions originally.

MSD_T10. This sub-dataset comes from the 10th sub-dataset of Medical Segmentation Decathlon [31] and features colon tumor segmentation.

<u>COLONOG.</u> This sub-dataset comes from the CT COLONOGRAPHY [16] dataset related to a CT colonography trial. It has prone and supine DICOM images for each patient. We randomly select one of two positions, which have the similar information, of each patient to our large dataset.

KITS19, CERVIX, ABDOMEN, MSD_T10, COLONOG, CLINIC, and CLINIC-metal are curated separately from different sites and sources and hence have a diverse range of spacing and FOV. The overview of our large dataset is shown in Table 1. In these sources, we exclude some cases of very low quality or without pelvic region and remove the unrelated areas outside the pelvis in our current dataset. At the same time, chyme, vascular sclerosis, coprolith, and other situations often encountered in the clinic also appear in these sub-datasets. Among them, the data of COLONOG, CLINIC, and CLINIC-metal are stored in a DICOM format, an international standard associated with transmitting, storing, and processing medical imaging information. However, not all data have the information about scanner manufacturer.

We reformat all DICOM images to NIfTI to simplify data processing and deidentify images, meeting the institutional review board (IRB) policies of contributing sites. All existing sub-datasets are under Creative Commons license CC-BY-NC-SA at least and we will keep the license unchanged. For CLINIC and CLINIC-metal sub-datasets, we will open-source them under Creative Commons license CC-BY-NC-SA 4.0. Further, we will add annotations of surgical planning and bones other than the pelvis to enrich our dataset.

2.2 Data Annotation

Considering the scale of thousands of cases in our dataset and annotation itself is truly a subjective and time-consuming task. We introduce a strategy of Annotation by Iterative Deep Learning (AID) [28] to speed up our annotation process. In the AID workflow, we train a deep network with a few precisely annotated

https://www.synapse.org/#!Synapse:syn3193805/wiki/89480

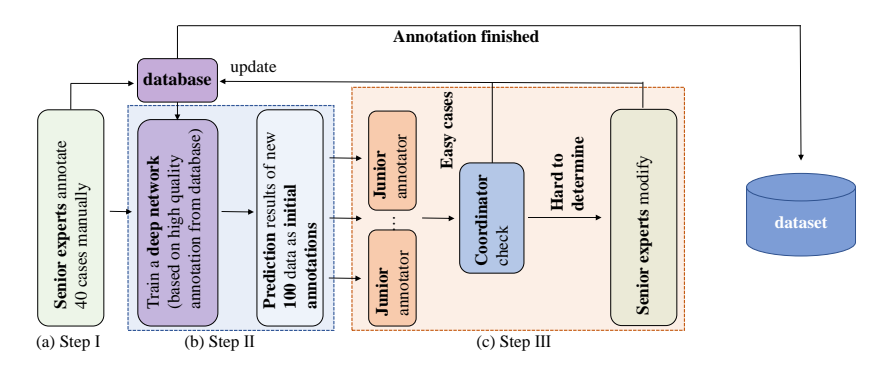


Fig. 2 The designed annotation pipeline based on an AID (Annotation by Iterative Deep Learning) strategy. In Step I, two senior experts first manually annotate 40 cases of data as the initial database. In Step II, we train a deep network based on the human annotated database and use it to predict new data. In Step III, initial annotations from the deep network are checked and modified by human annotators. Step II and Step III are repeated iteratively to refine a deep network to a more and more powerful 'annotator'. This deep network 'annotator' also unifies the annotation standards of different human annotators.

data in the beginning. Then the deep network is used to automatically annotate more data, followed by human experts' proofreading. The human-corrected annotations and their corresponding images are added to the training set to retrain a more powerful deep network. These steps are repeated iteratively until we finish our annotation task. In the last, only minimal modification is needed by human experts. Besides, when human experts correct the annotations based on the deep network's prediction, the annotation quality of different annotators becomes more consistent.

The annotation pipeline is shown in Fig. 2. In Step I, we invite two senior experts to pixel-wise annotate 40 cases of CLINIC sub-dataset precisely as the initial database. The reason for starting from the CLINIC sub-dataset is that the cancerous bone and surrounding tissues exhibit similar appearances at the fracture site, which needs more prior knowledge guidance from doctors. In Step II, we train a deep network with the updated database and make predictions on new 100 data at a time. In Step III, some junior annotators refine the labels based on the prediction results. A coordinator will check the quality of refinement by junior annotators. For easy cases, the annotation process is over in this stage; for hard cases, senior experts are invited to make more precise annotations. Step II and Step III are repeated until we finish the annotation of all images in our dataset. Finally, we conduct another round of visual scrutiny for outliers and mistakes and make necessary corrections to ensure the final quality of our dataset.

In total, we have annotations for 1,109 metal-free CTs and 14 metal-affected CTs. The remaining 61 metal-affected CTs of image are left unannotated and planned for use in unsupervised learning. We plan to make this dataset along with annotations open source.

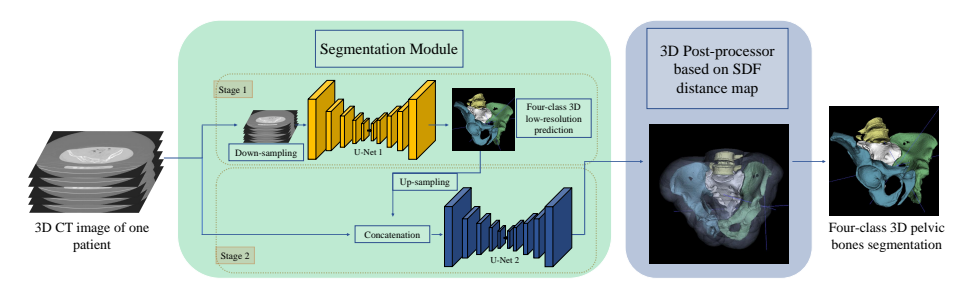


Fig. 3 Overview of our pelvic bones segmentation system, which learns from multi-domain CT images for effective and robust representations. The 3D U-Net cascade is used here to exploit more spatial information in 3D CT images. SDF is introduced to our post-processor to add distance constraint besides size constraint used in traditional MCR (maximum connected region) based method.

3 Segmentation Methodology

The overall pipeline of our deep pelvic bones segmentation approach is illustrated in Fig. 3. The input is a 3D CT image with multiple slices. (i) First, the input 3D CT image is sent to our multi-class 3D bones segmentation module. It is a plug and play (PnP) module that can be replaced at will. (ii) After segmentation is done, we send the multi-class 3D prediction to a SDF post-processor, which removes some false predictions and outputs the final multi-bone segmentation result.

3.1 Segmentation Module

Based on our large-scale dataset collected from multiple sources together with annotations, we use a fully supervised method to train a deep network to learn an effective representation of the pelvic bones. The deep learning framework we choose here is nnU-Net [15]. It is essentially a U-Net [29], but with specific network architecture design parameters and training parameters tuned to the characteristics of the dataset itself. Together with powerful data augmentation, nnU-Net [15] achieves better results than other deep learning methods in many of medical image segmentation tasks. Due to the huge amount of high-resolution 3D images in our dataset, choosing a 3D U-Net cascade [15] makes more sense here. 3D U-Net cascade contains two 3D U-net, where the first one is trained on downsampled images (stage 1 in Fig. 3), the second one is trained on full resolution images (stage 2 in Fig. 3). A 3D network can better exploit the useful 3D spatial information in 3D CT images. Training on downsampled images first can enlarge the size of patches in relation to the image, then also enable the 3D network to learn more contextual information. Training on full resolution images second refines the segmentation results predicted from former U-Net.

3.2 SDF Post Processor

Post-processing is useful for a stable system in clinical use, preventing some mispredictions in some complex scenes. In the segmentation task, current segmentation systems determine whether to remove the outliers according to the size of

Table 2 The Dice coefficient(DC) and Hausdorff distance(HD) results for different models tested on different datasets. 'Average' refers to the mean value of four anatomical structures' DC/HD. Sacrum, Left hip, Right hip, Lumbar spine refer to four different anatomical structures. 'Whole' refers to treating four anatomical structures as a whole bone. 'ALL' refers to the six metal-free sub-datasets excluding CLINIC-metal. The top three numbers in each part are marked in bold, red and blue.

Exp	Test	Model	Whole	Sacrum	Left hip	Right hip	Lumbar spine	Average
	(Dataset)	(Dataset)	Dice/HD	Dice/HD	Dice/HD	Dice/HD	Dice/HD	Dice/HD
(a)	ALL	$\Phi_{ALL(2.5D)}$.988/10.9	.979/19.6	.990/6.1	.990/5.5	.978/11.9	.984/10.8
	ALL	$\Phi_{ALL(3D)}$.988/12.2	.983/29.6	.988/9.8	.990/11.3	.982/10.6	.986/15.3
	ALL	$\Phi_{ALL(3D_cascade)}$.989/11.9	.984/18.7	.989/6.0	.991/5.6	.984/8.7	.987/9.76
(b)	ALL	$\Phi_{ABDOMEN}$.935/46.6	.675/88.0	.485/143.7	.473/141.1	.815/50.5	.612/105.8
,		$\Phi_{COLONOG}$.987/11.9	.982/26.6	.987/5.7	.989/6.6	.979/10.4	.984/12.3
		Φ_{MSD_T10}	.910/52.9	.512/79.3	.521/135.5	.541/137.7	.555/60.8	.532/103.4
		Φ_{KITS19}	.939/37.9	.691/68.4	.648/103.6	.645/103.2	.887/56.1	.718/82.9
		Φ_{CERVIX}	.979/23.2	.963/53.1	.975/35.3	.978/36.0	.967/27.8	.971/38.1
		Φ_{CLINIC}	.947/30.9	.690/71.0	.622/104.4	.646/103.4	.859/38.6	.704/79.4
		Φ_{ALL}	.989/11.9	.984/18.7	.989/6.0	.991/5.6	.984/8.7	.987/9.76
	ABDOMEN	$\Phi_{ABDOMEN}$.982/8.2	.973/7.3	.985/1.6	.985/2.0	.973/4.9	.979/4.0
		$\Phi_{COLONOG}$.972/12.5	. <mark>968</mark> /36.0	.979/2.3	.981/2.3	.937/29.4	.966/17.5
		Φ_{MSD_T10}	.981/5.1	.974/4.5	.983/1.7	.985/1.8	.973/3.9	.979/3.0
		Φ_{KITS19}	.858/36.6	.325/58.0	.219/175.5	.262/180.3	.678/61.8	.371/118.9
		Φ_{CERVIX}	.972/11.3	.957/12.5	.979/3.5	.980/2.7	. <mark>951</mark> /17.8	.967/9.1
		Φ_{CLINIC}	.883/30.2	.271/94.6	.144/175.5	.278/178.2	.678/37.9	.343/121.6
		Φ_{ALL}	.981/5.2	.974/3.9	.984/1.6	.985/1.9	.973/4.2	.979/2.9
		$\Phi_{ex~ABDOMEN}$.980/4.2	.973/3.3	.982/1.7	.984/1.9	.973/4.2	.978/2.8
	COLONOG	$\Phi_{ABDOMEN}$.928/55.5	.661/107.4	.440/163.2	.431/158.9	.793/57.6	.581/121.8
		$\Phi_{COLONOG}$.989/10.5	.988/30.4	.989/4.3	.992/6.3	.988/8.7	.989/12.4
		Φ_{MSD_T10}	.904/59.4	.504/91.6	.467/152.2	.495/154.2	.531/66.7	.499/116.2
		Φ_{KITS19}	.947/42.4	.737/81.2	.680/106.4	.666/106.0	.908/63.3	.748/89.2
		Φ_{CERVIX}	.980/27.1	.963/70.5	.972/45.7	.975/46.1	.973/35.0	.971/49.3
		Φ_{CLINIC}	.956/33.6	.730/79.9	.650/107.4	.658/107.4	.892/46.6	.732/85.3
		Φ_{ALL}	.990/11.7	.988/21.6	.989/5.9	.992/5.8	.988/9.0	.989/10.0
	AGD THO	$\Phi_{ex\ COLONOG}$.988/13.1	.981/34.2	.988/8.4	.991/6.3	.982/12.5	.986/15.4
	MSD_T10	$\Phi_{ABDOMEN}$.984/5.5	.977/9.4	.988/2.1	.988/2.7	.967/6.0	.980/5.1
		$\Phi_{COLONOG}$.982/6.4	.975/12.4	.983/4.5	.985/4.0	.972/7.3	.979/7.0
		Φ_{MSD_T10}	.989/5.1	.984/9.3	.991/1.9	.991/2.4	.981/4.5	.987/4.6
		Φ_{KITS19}	.860/38.8 .974/9.4	.210/76.5	.171/190.7	.203/192.3	.736/76.8 .954/14.1	.330/134.1
		Φ_{CERVIX}		.957/20.8 .240/85.3	.977/21.4	.979/30.3		.967/21.6
		Φ_{CLINIC}	.873/27.6 .989/4.3	.984/4.2	.137/188.2	.244/186.2	.603/31.8	.306/122.9
		Φ_{ALL}	.986/4.6	.984/4.2	.990/2.2 .988/2.6	.990/ 2.4 .989/2.5	.981/4.3 .977/6.4	.987/3.3 .984/5.1
	KITS19	$\Phi_{ex\ MSD_T10}$ $\Phi_{ABDOMEN}$.926/57.2	.585/112.5	0.118/243.0	0.100/243.0	.756/70.2	.390/167.2
	KIIDID	$\Phi_{COLONOG}$.985/15.7	.983/17.2	.988/12.0	.988/12.8	.970/12.1	.982/13.5
-		Φ_{MSD_T10}	.854/78.0	.106/108.0	.245/242.8	.260/242.9	.245/76.2	.214/167.5
		Φ_{KITS19}	.988/10.6	.984/8.1	.989/3.6	.990/4.3	.981/7.9	.986/6.0
		Φ_{CERVIX}	.983/15.7	.980/16.3	.988/12.9	.988/4.8	.962/12.7	.979/11.7
		Φ_{CLINIC}	.986/23.4	.983/32.8	.987/13.5	.989/10.3	.978/10.0	.984/16.6
		Φ_{ALL}	.987/11.3	.983/22.7	.989/4.0	.989/4.2	.978/9.2	.985/10.0
		$\Phi_{ex\ KITS19}$.985/14.5	.983/12.7	.988/13.0	.988/13.3	.971/10.9	.983/12.5
	CERVIX	$\Phi_{ABDOMEN}$.922/26.5	.512/40.8	.057/148.4	.046/149.5	.711/42.5	.332/95.3
		$\Phi_{COLONOG}$.981/9.4	.960/7.9	.984/2.0	.984/2.4	.946/8.4	.969/5.2
		Φ_{MSD_T10}	.881/34.4	.053/53.1	.112/148.8	.105/149.4	.163/54.4	.108/101.4
		Φ_{KITS19}	.982/9.8	.967/8.8	.984/2.0	.984/2.8	.955/7.0	.973/5.1
		Φ_{CERVIX}	.983/8.8	.967/7.4	.986/1.9	.985/2.1	.955/6.9	.973/4.6
		Φ_{CLINIC}	.977/13.0	.955/16.8	.984/9.5	.984/4.7	.950/19.4	.968/12.6
		Φ_{ALL}	.982/9.1	.965/8.0	.985/1.9	.985/2.6	.953/7.6	.972/5.0
		$\Phi_{ex\ CERVIX}$.982/9.6	.970/8.0	.985/1.8	.985/2.5	.961/7.4	.975/4.9
	CLINIC	$\Phi_{ABDOMEN}$.905/62.7	.337/107.1	.227/220.6	.171/220.9	.755/77.6	.372/156.0
		$\Phi_{COLONOG}$.983/29.6	.960/30.4	.986/17.5	.985/12.9	.963/20.3	.973/20.3
		Φ_{MSD_T10}	.844/91.3	.082/121.6	.338/210.5	.357/218.9	.255/118.4	.258/167.
		Φ_{KITS19}	.985/29.5	.964/23.2	.988/18.0	.987/12.0	.966/16.3	.976/17.4
		Φ_{CERVIX}	.981/30.0	.962/29.8	.986 18.7	.985/13.9	.963/17.2	.974/19.9
		Φ_{CLINIC}	.987/28.2	.976/20.3	.989/16.5	.989/11.3	.977/14.2	.983/15.0
		Φ_{ALL}	.986/28.9	.974/28.2	.989/16.9	.988/12.0	.976/14.3	.982/17.9
		$\Phi_{ex\ CLINIC}$.984/28.7	.963/28.6	.987/17.5	.985/12.2	.963/20.2	.974/19.6
(c)	CLINIC-metal	Φ_{ALL}	.933/50.8	941/80.5	.943/68.1	.928/41.1	.906/36.6	.929/56.6

the connected region to reduce mispredictions. However, in the pelvic fractures scene, broken bones may also be removed as outliers. To this end, we introduce the signed distance function (SDF) [27] filtering as our post-processing module to add a distance constraint besides the size constraint. We calculate SDF based on the maximum connected region (MCR) of each anatomical structure in the prediction result. Through some simple mathematical calculations such as truncation, we obtain a 3D distance map that decreases from the bone border to the image boundary. We set a distance threshold and a region threshold to determine whether 'outlier prediction' defined by traditional maximum connected region-based method should be removed (Sect. 4.2.2).

4 Experiments

4.1 Implementation Details

We implement our method using PyTorch⁴ and MONAI⁵. For segmenator, we keep the training configuration, such as loss function and learning rate schedule, etc., the same as nnU-Net⁶ [15], excluding mirror flipping operation in data augmentation. Although pelvic bone is an anatomically symmetrical structure itself, the pelvic cavity is not. For example, the sigmoid colon only appears on the left side of the body. We mainly focus on the pelvic bone structure, but it is equally important to retain information about the surrounding organs. Because the sacroiliac and lumbosacral joints only occupy a small area of the pelvis, we also increase their sampling rate in the sampling strategy during training. For our metal-free dataset, we randomly select 3/5, 1/5, 1/5 cases in each sub-dataset as the training set, validation set, and testing set, respectively, and keep such a data partition unchanged in all-dataset experiments and sub-datasets experiments.

4.2 Results and Discussion

4.2.1 Segmentation Module

To prove that learning from our large-scale pelvic bones CT dataset is helpful to improve the robustness of our segmentation system, we conduct a series of experiments in different aspects.

Performance of baseline models. Firstly, we test the performance of models of different dimensions on our entire dataset. The Exp (a) in Table 2 shows the quantitative results. In Table 2, Dataset 'ALL' refers to the six metal-free subdatasets mentioned above, except the CLINIC-metal sub-dataset. $\Phi_{dataset\ name}$ denotes a deep network model trained on the corresponding dataset, ie., Φ_{ALL} , $\Phi_{ABDOMEN}$, etc. Following the conventions in most literature, we use Dice coefficient(DC) and Hausdorff distance (HD) as the metrics for quantitative evaluation. All results are tested on our testing set. Same as we discussed in Sect. 3.1, $\Phi_{ALL(3D_cascade)}$ shows the best performance, achieving an average DC of 0.987 and HD of 9.76, because it utilizes more 3D spatial information with a larger receptive field than other models. As the following experiments are all trained with 3D U-Net cascade, the mark $(3D_cascade)$ of $\Phi_{ALL(3D_cascade)}$ is omitted for notational clarity.

Generalization across sub-datasets. Secondly, we train six deep networks, one network per single sub-dataset ($\Phi_{ABDOMEN}$, $\Phi_{COLONOG}$, Φ_{MSD_T10} , Φ_{KITS19} , Φ_{CERVIX} , Φ_{CLINIC}). Then we test them on each sub-dataset to verify the effectiveness of our large-scale dataset, pooled from multiple domains. Quantitative and qualitative results are shown in Exp (b) in Table 2 and Fig. 4, respectively. We also calculate the performance of Φ_{ALL} on each sub-dataset. For a fair comparison, cross-testing of sub-dataset networks is also conducted on each sub-dataset's

 $^{^4}$ pytorch.org

⁵ monai.io

 $^{^{6} \ {\}tt github.com/mic-dkfz/nnunet}$



Fig. 4 Visualization of segmentation results from six datasets. Six rows refer to six images from six metal-free sub-datasets tested on different models.

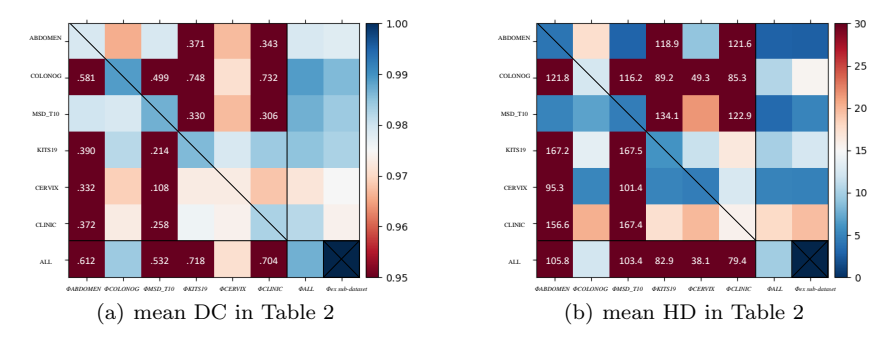


Fig. 5 Heat map of mean DC & HD results in Table 2. The vertical axis represents different sub-datasets and the horizontal axis represents different models. In order to show the normal values more clearly, we clip some outliers to the boundary value, i.e., 0.95 in DC and 30 in HD. The values out of range are marked in the grid. The cross in the lower right corner indicates that there is no corresponding experiment.

testing set. We observe that the evaluation metrics of model Φ_{ALL} are generally better than those for the model trained on a single sub-dataset. These models trained on a single sub-dataset are difficult to consistently perform well in other domains, except $\Phi_{COLONOG}$, which contains the largest amount of data from various sources, originally. This observation implies that the domain gap problem does exist and the solution of collecting data directly from multi-source is effective. More intuitively, we show the 'Average' values in heat map format in Fig. 5.

Furthermore, we implement leave-one-out cross-validation of these six metalfree sub-datasets to verify the generalization ability of this solution. Models are marked as $\Phi_{ex\ ABDOMEN}$, etc. The results of $\Phi_{ex\ COLONOG}$ can fully explain that training with data from multi-sources can achieve good results on data that has not been seen before. When the models trained separately on the other five

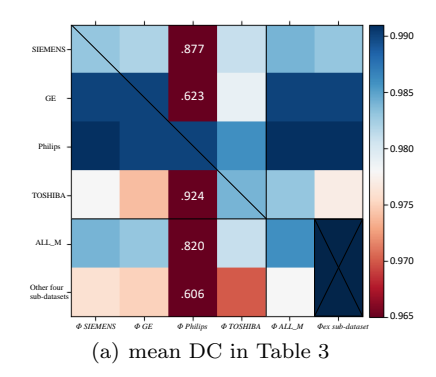
Table 3 (a) The Dice coefficient(DC) and Hausdorff distance(HD) results for different models tested on different datasets from different manufacturers. 'ALL_M' refers to that all data of manufacturer information can be accessed. (b) Effect of different post-processing methods on 'ALL' dataset. The top three numbers in each part are marked in bold, red and blue.

Exp	Test	Model	Whole	Sacrum	Left hip	Right hip	Lumbar spine	Average
	(Dataset)	(Dataset)	Dice/HD	Dice/HD	Dice/HD	Dice/HD	Dice/HD	Dice/HD
(a)	SIEMENS	$\Phi_{SIEMENS}$.991/10.9	.985/29.4	.981/7.4	.982/6.0	.984/9.5	.983/13.1
		Φ_{GE}	.990/11.1	.983/24.4	.981/7.7	.981/6.1	.985/11.0	.982/12.3
		$\Phi_{Philips}$.981/17.2	.917/33.0	.824/63.5	.803/63.5	.966/28.8	.877/47.2
		$\Phi_{TOSHIBA}$.990/11.1	.983/28.8	.981/7.5	.982/8.6	.980/11.2	.981/14.0
		Φ_{ALL_M}	.991/10.3	.985/19.1	.981/7.3	.983/6.0	.985/10.1	.984/10.6
		$\Phi_{ex\ SIEMENS}$.991/11.0	.986/22.1	.981/7.4	.982/6.0	.985/10.1	.983/11.4
	GE	$\Phi_{SIEMENS}$.991/9.6	.988/35.7	.992/3.9	.992/4.3	.988/8.5	.990/13.1
		Φ_{GE}	.991/9.8	.988/17.3	.992/4.0	.992/6.7	.988/8.0	.990/9.0
		$\Phi_{Philips}$.949/41.3	.721/95.7	.443/198.2	.401/200.5	.925/93.7	.623/147.0
		$\Phi_{TOSHIBA}$.982/22.1	.967/60.4	.984/28.5	.985/24.8	.979/40.6	.979/38.6
		Φ_{ALL_M}	.991/9.1	.989/27.6	.992/3.8	.992/6.5	.988/7.9	.990/11.5
		$\Phi_{ex~GE}$.990/9.8	.987/23.9	.992/4.0	.992/6.7	.987/8.8	.990/10.8
	Philips	$\Phi_{SIEMENS}$.992/6.4	.988/6.8	.993/2.8	.993/2.8	.990/2.0	.991/3.6
		Φ_{GE}	.991/7.8	.987/8.4	.993/2.6	.993/3.4	.989/3.1	.990/4.4
		$\Phi_{Philips}$.991/6.4	.987/7.7	993/2.9	993/4.1	.989/2.8	.990/4.4
		$\Phi_{TOSHIBA}$.991/15.9	.984/42.4	.985/11.0	.986/35.3	.989/39.6	.986/32.1
		Φ_{ALL_M}	.992/7.0	.988/7.4	.993/2.6	.993/3.1	.990/2.2	.991/3.8
		$\Phi_{ex\ Philips}$.992/6.8	.988/7.0	.993 /3.0	.993/3.0	.990/2.1	.991/3.8
	TOSHIBA	$\Phi_{SIEMENS}$.985/25.9	.966/31.2	.988/15.8	.988/9.7	.969/16.6	.978/18.3
		Φ_{GE}	.983/30.3	.961/45.0	.987/21.9	.987/20.2	.962/25.2	.974/28.1
		$\Phi_{Philips}$.981/28.0	.945/40.0	.894/47.0	.900/47.2	.959/38.5	.924/43.2
		$\Phi_{TOSHIBA}$.988/25.3	.978/36.0	.990/14.4	.989/10.6	.979/13.4	.984/18.6
		Φ_{ALL_M}	.987/26.3	.976/29.3	.989/14.5	.988/11.2	.978/15.0	.983/17.5
		$\Phi_{ex\ TOSHIBA}$.985/25.8	.965/38.0	.988/16.1	.988/9.9	.969/16.4	.977/20.1
	ALL_M	$\Phi_{SIEMENS}$.990/12.7	.983/30.7	.986/7.6	.986/6.0	.983/10.1	.984/13.6
		Φ_{GE}	.989/13.6	.981/25.2	.985/8.7	.985/8.4	.982/12.2	.983/13.6
		$\Phi_{Philips}$.973/25.0	.871/49.9	.739/94.8	.717/95.5	.955/46.7	.820/71.7
		$\Phi_{TOSHIBA}$.988/16.4	.978/38.7	.984/14.3	.984/14.0	.980/20.2	.981/21.8
		Φ_{ALL_M}	.991/12.4	.985/22.6	.986/7.3	.986/6.8	.985/10.1	.986/11.7
	Other four	$\Phi_{SIEMENS}$.981/8.8	.972/25.3	.984/3.8	.985/7.1	.965/10.8	.976/11.8
	sub-datasets	Φ_{GE}	.980/9.8	.971/41.2	.984/4.7	.985/4.3	.961/16.2	.975/16.6
		$\Phi_{Philips}$.896/38.0	.526/81.2	.568/130.5	.565/129.4	.765/76.3	.606/104.3
		$\Phi_{TOSHIBA}$.976/15.2	.964/25.2	.981/7.7	.981/7.2	.952/17.9	.970/14.5
		Φ_{ALL_M}	.982/8.4	.975/18.9	.984/3.0	.985/5.4	.969/6.3	.978/8.4
(b)	w/o Post	Φ_{ALL}	.988/37.5	.984/44.2	.984/36.1	.986/30.6	.983/13.1	.984/31.0
` '	MCR	Φ_{ALL}	.988/14.5	.984/18.9	.989/6.3	.990/6.9	.978/11.4	.985/10.9
	SDF(0.20)	Φ_{ALL}	.989/12.0	.984/19.3	.989/6.0	.991/5.5	.983/9.4	.987/10.1
	SDF(0.25)	Φ_{ALL}	.989/11.9	.984/18.7	.989/6.0	.991/5.6	.984/8.7	.987/9.76
	SDF(0.30)	Φ_{ALL}	.989/12.2	.984/18.7	.989/6.0	.991/5.6	.983/8.9	.987/9.82
	SDF(0.35)	Φ_{ALL}	.989/12.6	.984/18.7	.989/6.0	.991/5.6	.982/9.7	.987/10.0
	222 (3.00)	- ALL	/12.0	/1011	/010	/ 0.0		/10.0

sub-datasets cannot achieve good results on COLONOG, aggregating these five sub-datasets can get a comparable result compared with Φ_{ALL} . More data from multi-sources can be seen as additional constraints on model learning, prompting the network to learn better feature representations of the pelvic bones and the background. In Fig. 4, the above discussions can be seen intuitively through qualitative results.

Generalization across manufacturers. Finally, as shown in Exp (a) in Table 3, to further illustrate the impact of different domains on our system performance, we conduct experiments based on data produced by different equipment manufacturers. By reading the meta-information saved in the header of DICOM files, we select out 449, 218, 25, 125 images of Siemens, GE, Philips, and Toshiba, respectively, from the COLONOG and CLINIC sub-datasets.

 $\Phi_{ABDOMEN}$ in Table 2 and $\Phi_{Philips}$ in Table 3 indicate that a few numbers of CTs is enough to train a deep learning model applying to their own domain, but with poor generalization performance. $\Phi_{TOSHIBA}$, Φ_{GE} , and $\Phi_{SIEMENS}$ indicate that increasing the number of dataset of one single domain can improve generalization performance. $\Phi_{ex\ COLONOG}$, and $\Phi_{ex\ SIEMENS}$ imply that aggregating multi-source CTs can also improve generalization performance even with less number of CTs. $\Phi_{COLONOG}$ (with multi-source CTs), Φ_{ALL} and Φ_{ALL_M} show more sources and more data make the model perform better. Intuitive heat map of 'Average' values are shown in Fig. 6.



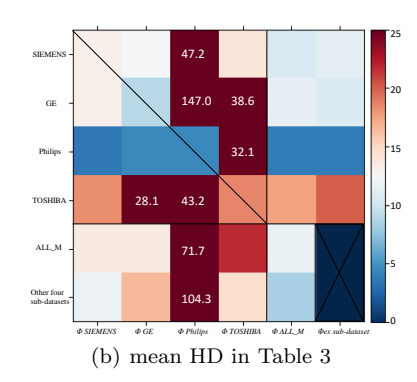


Fig. 6 Heat map of mean DC & HD results in Table 3. The vertical axis represents different sub-datasets and the horizontal axis represents different models. Boundary values here are 0.965 in DC and 30 in HD.

'Whole' vs 'Average'. In addition, comparing 'Whole' and 'Average' columns in Table 2 and Table 3, we find that some models that do not perform well in 'Average' metric are not so bad in 'Whole' metric, which means multi-class segmentation is harder than binary segmentation. The presence of multiple classes introduces more granularity and complexity and hence makes the segmentation more challenging.

Metal-affected image segmentation. Because a CT image with metal artifacts in CLINIC-metal sub-dataset is special, ground truth labeling is difficult and its appearance distribution is quite different from that of normal CT. We treat this situation separately from other conditions to avoid impact on other metal-free data. In our dataset, we only annotate 14 CTs as testing set. The results of these 14 CTs under our automatic segmentation system is shown in Exp (c) in Table 2. Poor 'Whole' and 'Average' results all show the segmentation challenge. How to deal with such difficult cases is a future direction we plan to study. We also collect 61 other metal-affected CTs in our large-scale dataset. It is expected that good segmentation results can be obtained directly or indirectly through unsupervised methods [21], such as direct learning of segmentation features or metal artifact reduction first.

4.2.2 SDF post-processor

The Exp (b) in Table 3 shows the effect of the post-processing module. The performance of the system that includes the SDF post-processing module is consistently better than the system without the post-processing module and with the MCR module. Through comparative experiments, we choose 0.25 as the optimal distance field threshold. In these experiments, we only keep a reasonable connected region with an area bigger than 2000 voxels. SDF yields a decrease of 1.14 (10.5%) in HD value and 0.002 in DC in all testing sets compared with MCR post-processor. The SDF post-processor is mainly designed for the pelvic fracture scene, because in the case of a complete pelvis (sub-datasets excluding CLINIC), the performance of the SDF post-processor is the same as the MCR post-processor. The visual effects of two cases are displayed in Fig. 7. Large fragments near the anatomical structure are kept with SDF post-processing but are removed by the MCR method.

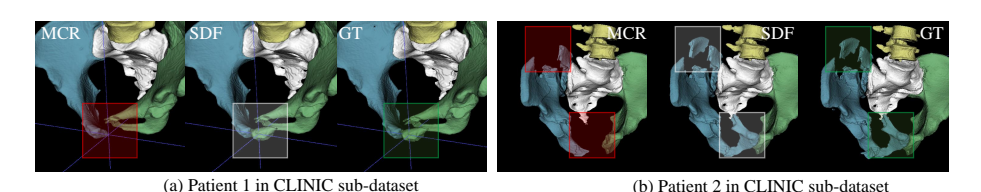


Fig. 7 Comparison between post-processing methods: traditional MCR and the proposed SDF filtering.

5 Conclusion

To benefit the pelvic surgery and diagnosis community, we curate a large-scale pelvic CT dataset pooled from multiple domains, including 1,184 CT volumes (over 320K CT slices) of various appearance variations, and present a pelvic segmentation system based on deep learning, which, to the best of our knowledge, marks the first attempt in the literature. We train a multi-class network for segmentation of lumbar spine, sacrum, left hip, and right hip using the multiple-domain images to obtain more effective and robust features. SDF filtering further improves the robustness of the system. This system lays a solid foundation for our future work. We plan to open source the datasets, test the significance of our system in real clinical practices, and explore more options based on our dataset, e.g. devising a module for metal-affected CTs and domain-independent pelvic bones segmentation algorithm.

References

- Aguirre-Ramos, H., Avina-Cervantes, J.G., Cruz-Aceves, I.: Automatic bone segmentation by a gaussian modeled threshold. In: AIP Conference Proceedings. vol. 1747, p. 090009. AIP Publishing LLC (2016)
- Barratt, R.C., Bernard, J., Mundy, A.R., Greenwell, T.J.: Pelvic fracture urethral injury in males—mechanisms of injury, management options and outcomes. Translational Andrology and Urology 7(Suppl 1), S29 (2018)
- 3. Chandar, K.P., Satyasavithri, T.: Segmentation and 3d visualization of pelvic bone from ct scan images. In: IACC. pp. 430–433. IEEE (2016)
- 4. Chen, C., Zheng, G.: Fully automatic segmentation of AP pelvis x-rays via random forest regression and hierarchical sparse shape composition. In: Intl. Conf. on Computer Analysis of Images and Patterns. pp. 335–343. Springer (2013)
- 5. Chen, L.C., Zhu, Y., et al.: Encoder-decoder with atrous separable convolution for semantic image segmentation. In: ECCV. pp. 801–818 (2018)
- 6. Çiçek, Ö., Abdulkadir, A., et al.: 3D U-Net: learning dense volumetric segmentation from sparse annotation. In: MICCAI. pp. 424–432. Springer (2016)
- 7. Dechert, T., Duane, T., et al.: Elderly patients with pelvic fracture: Interventions and outcomes. The American Surgeon **75**, 291–5 (05 2009). https://doi.org/10.1177/000313480907500405
- 8. Ding, F., Leow, W.K., Howe, T.S.: Automatic segmentation of femur bones in anterior-posterior pelvis x-ray images. In: International Conference on Computer Analysis of Images and Patterns. pp. 205–212. Springer (2007)
- Gibson, E., Giganti, F., et al.: Automatic multi-organ segmentation on abdominal CT with dense v-networks. IEEE Transactions on Medical Imaging 37(8), 1822–1834 (2018)
- 10. Grotz, M., Allami, M., et al.: Open pelvic fractures: epidemiology, current concepts of management and outcome. Injury 36(1), 1–13 (2005)

- Guo, Q., Zhang, L., et al.: Clinical features and risk factors for mortality in patients with open pelvic fracture: A retrospective study of 46 cases. Journal of Orthopaedic Surgery 28(2), 2309499020939830 (2020)
- 12. Haas, B., Coradi, T., et al.: Automatic segmentation of thoracic and pelvic CT images for radiotherapy planning using implicit anatomic knowledge and organ-specific segmentation strategies. Physics in Medicine & Biology **53**(6), 1751 (2008)
- 13. Heller, N., Sathianathen, N., et al.: The kits19 challenge data: 300 kidney tumor cases with clinical context, CT semantic segmentations, and surgical outcomes. arXiv:1904.00445 (2019)
- Hemke, R., Buckless, C.G., et al.: Deep learning for automated segmentation of pelvic muscles, fat, and bone from CT studies for body composition assessment. Skeletal Radiology 49(3), 387–395 (2020)
- 15. Isensee, F., Jäger, P.F., et al.: Automated design of deep learning methods for biomedical image segmentation. arXiv preprint arXiv:1904.08128 (2019)
- Johnson, C.D., Chen, M.H., et al.: Accuracy of CT colonography for detection of large adenomas and cancers. New England Journal of Medicine 359(12), 1207–1217 (2008)
- Kainmueller, D., Lamecker, H., et al.: Coupling deformable models for multi-object segmentation. In: ISBI. pp. 69–78. Springer (2008)
- 18. Kotlarsky, P., Haber, R., Bialik, V., Eidelman, M.: Developmental dysplasia of the hip: What has changed in the last 20 years? World Journal of Orthopedics 6(11), 886 (2015)
- Lamecker, H., Seebass, M., Hege, H.C., Deuflhard, P.: A 3D statistical shape model of the pelvic bone for segmentation. vol. 5370, pp. 1341–1351. International Society for Optics and Photonics (2004)
- Lee, P.Y., Lai, J.Y., et al.: Virtual 3D planning of pelvic fracture reduction and implant placement. Biomedical Engineering: Applications, Basis and Communications 24(03), 245– 262 (2012)
- Liao, H., Lin, W.A., Zhou, S.K., Luo, J.: ADN: Artifact disentanglement network for unsupervised metal artifact reduction. IEEE Transactions on Medical Imaging 39(3), 634– 643 (2019)
- 22. Lindner, C., Thiagarajah, S., et al.: Accurate fully automatic femur segmentation in pelvic radiographs using regression voting. In: MICCAI. pp. 353–360. Springer (2012)
- Lindner, C., Thiagarajah, S., et al.: Fully automatic segmentation of the proximal femur using random forest regression voting. IEEE Transactions on Medical Imaging 32(8), 1462–1472 (2013)
- Long, J., Shelhamer, E., Darrell, T.: Fully convolutional networks for semantic segmentation. In: CVPR. pp. 3431–3440 (2015)
- Mostafavi, H.R., Tornetta III, P.: Radiologic evaluation of the pelvis. Clinical Orthopaedics and Related Research (1976-2007) 329, 6–14 (1996)
- Pasquier, D., Lacornerie, T., et al.: Automatic segmentation of pelvic structures from magnetic resonance images for prostate cancer radiotherapy. International Journal of Radiation Oncology* Biology* Physics 68(2), 592–600 (2007)
- 27. Perera, S., Barnes, N., et al.: Motion segmentation of truncated signed distance function based volumetric surfaces. In: WACV. pp. 1046–1053. IEEE (2015)
- 28. Philbrick, K.A., Weston, A.D., et al.: Ril-contour: a medical imaging dataset annotation tool for and with deep learning. Journal of Digital Imaging 32(4), 571–581 (2019)
- 29. Ronneberger, O., Fischer, P., Brox, T.: U-net: Convolutional networks for biomedical image segmentation. In: MICCAI. pp. 234–241. Springer (2015)
- Seim, H., Kainmueller, D., et al.: Automatic segmentation of the pelvic bones from CT data based on a statistical shape model. VCBM 8, 93–100 (2008)
- 31. Simpson, A.L., Antonelli, M., et al.: A large annotated medical image dataset for the development and evaluation of segmentation algorithms. arXiv:1902.09063 (2019)
- 32. Truc, P.T., Lee, S., Kim, T.S.: A density distance augmented chan-vese active contour for CT bone segmentation. In: Intl. Conf. of the IEEE Engineering in Medicine and Biology Society. pp. 482–485. IEEE (2008)
- 33. Vasilache, S., Ward, K., Cockrell, C., Ha, J., Najarian, K.: Unified wavelet and gaussian filtering for segmentation of CT images; application in segmentation of bone in pelvic CT images. BMC Medical Informatics and Decision Making 9(1), 1–8 (2009)
- 34. Wu, J., Hargraves, R.H., et al.: Segmentation and fracture detection in CT images (Nov 1 2016), US Patent 9,480,439
- Yu, H., Wang, H., et al.: The segmentation of bones in pelvic CT images based on extraction of key frames. BMC medical imaging 18(1), 18 (2018)

Zhao, H., Shi, J., Qi, X., Wang, X., Jia, J.: Pyramid scene parsing network. In: CVPR. pp. 2881–2890 (2017)
 Zhou, Y., Xie, L., Fishman, E.K., Yuille, A.L.: Deep supervision for pancreatic cyst segmentation in abdominal CT scans. In: MICCAI. pp. 222–230. Springer (2017)